

Massachusetts Institute of Technology
Department of Mechanical Engineering
Cambridge, MA 02139

2.002 Mechanics and Materials II
Spring 2004

Laboratory Module No. 4
Isotropic Linear Elastic Stress Concentration

1 Objectives

The primary objectives of this lab are to introduce the concept of stress and strain concentration factors in notched structural configurations. The notion of stress concentration is experimentally explored qualitatively, using photoelasticity, and quantitatively, using experimental, analytical, and numerical methods.

We will first examine photoelastic stress analysis techniques to illustrate features of locally concentrated stress and strain distributions around notches, holes, fillets, and other geometric discontinuities. We will then present analytical solutions for the stress distribution around a circular hole in an infinite plate, subjected to remote tensile loading, and quantitatively introduce the concept of a stress concentration factor. Estimates of the stress concentration factor for various notch geometries will be obtained from approximate engineering solutions. We will then measure the strain distributions around a circular hole, using standard strain gauge techniques. Finally, we will examine modern numerical solutions of the underlying elasticity problem, based on the finite element method.

2 Lab Tasks

In this laboratory module we will

- review the concepts of linear elastic stress concentration factors associated with geometric discontinuities such as notches, holes, and cut-outs
- quantitatively examine the analytical stress fields around an isolated circular hole in a large (infinite) plate subject to remote uniaxial tension
- generalize the concept of stress concentration factor to finite bodies, and explore the consequences of St. Venant's principle for using analytical "infinite body" stress concentration results to estimate stress concentration associated with isolated discontinuities
- discuss basics of photoelastic stress analysis of transparent birefringent materials
- subject notched specimens of aluminum 6061-T6 and the engineering polymer polycarbonate (PC) to uniaxial elastic-level loading, and perform experimental evaluation of the stress concentration factor by using strain gauge output taken from the aluminum specimen, and birefringence contours observed on the PC.
- examine basic output numerical results from a linear elastic plane stress finite element solution of the loaded notched specimen.

3 Lab Assignments: Specific Questions to Answer

1. For the case of a circular hole in an infinitely wide plate, using equations (1a, 1b, 1c), derive analytical expressions for the distribution of the stress components σ_{rr} , $\sigma_{\theta\theta}$, and $\sigma_{r\theta}$ as a function of radial coordinate, r , along the ligament (the axis normal to remote loading, with $\theta = \pi/2$; the sign convention for θ is given in Fig. 1). Plot these stress values, normalized by the far-field stress σ , for the range $a \leq r \leq 10a$. At what relative distance (r/a) does the value of $\sigma_{\theta\theta}$ return to within 5% of the applied far-field stress? How does this compare with St. Venant's principle?
2. For the case of a circular hole in a finite-width plate, and in particular, for the geometry of the specimen in Fig 8a, obtain the value of the stress concentration factor K_{tg} from the graph in Fig. 3. Compare the level of $\sigma_{\theta\theta}/\sigma$ at the edge of the hole ($r = a$) in an infinite plate, computed in (1) above, to that of the finite-width plate. Explain the reasons for any differences between the two stress concentration factor values.
3. During the lab session, local circumferential strain values, $\epsilon_{\theta\theta}$, were recorded at various strain gauges placed along the ligament ($\theta = \pi/2$). Plot these measured strain values as a function of the radial coordinate r , measured from the center of the hole.
4. An additional remote strain gauge measured the far-field axial strain. Using this measurement, estimate the strain concentration factor at the hole, K_ϵ (see eq. (13)). How does K_ϵ compare with K_{tg} obtained in (2) above? Comment on the similarity/difference between the two values.
5. Using the analytical expressions for σ_{rr} , $\sigma_{\theta\theta}$, and $\sigma_{r\theta}$ derived in (1) above, obtain an analytical expression for the radial distribution of strain, $\epsilon_{\theta\theta}$, on the ligament at $\theta = \pi/2$. Use this expression to obtain an approximate prediction of the $\epsilon_{\theta\theta}$ profile along the ligament of the finite aluminum plate in Fig. 8a. The plate is loaded with an axial force $P = 40kN$. In your calculations, assume a value for the Young's modulus of the aluminum plate as $E = 72GPa$, and Poisson ratio of $\nu = 0.32$. Compare your predictions with the experimental values obtained in (3) above, and comment on possible sources for differences between the measurements and the prediction.
6. Compare the experimental values of strain on the ligament of the aluminum specimen with values obtained from the finite element simulation. What value does the finite element solution give for the strain concentration factor, K_ϵ ?
7. Comment on any observations made in the PC stress/strain concentration configuration experiments. What effect did various geometric stress concentrators have on the deformation of the material?

4 Background on Linear Elastic Stress Concentration

4.1 Circular hole in an infinite plate under remote tensile load

The stress distributions around a central hole can be estimated for the simple case of an infinitely wide plate subjected to tensile loading. The overall stress distributions in the plate are given by (Figure 1)

$$\sigma_{rr}(r, \theta) = \frac{\sigma}{2} \left[\left(1 - \frac{a^2}{r^2}\right) + \left(1 + 3\frac{a^4}{r^4} - 4\frac{a^2}{r^2}\right) \cos(2\theta) \right] \quad (1a)$$

$$\sigma_{\theta\theta}(r, \theta) = \frac{\sigma}{2} \left[\left(1 + \frac{a^2}{r^2}\right) - \left(1 + 3\frac{a^4}{r^4}\right) \cos(2\theta) \right] \quad (1b)$$

$$\sigma_{r\theta}(r, \theta) = -\frac{\sigma}{2} \left[\left(1 - 3\frac{a^4}{r^4} + 2\frac{a^2}{r^2}\right) \sin(2\theta) \right] \quad (1c)$$

where “ σ ” is the magnitude of the remotely-applied tensile stress, σ_{xx}^{∞} .

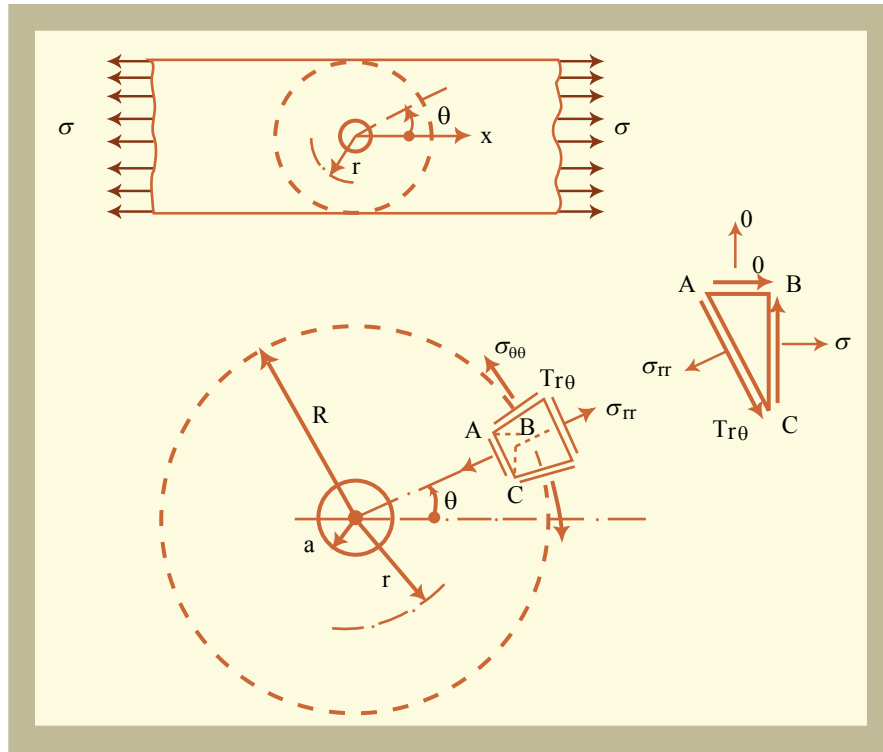


Figure 1: Stress distribution around a circular hole.

The surface of the circular hole is $r = a$; the unit normal to this surface is $\mathbf{n} = -\mathbf{e}_r$, where \mathbf{e}_r is the unit vector in the local radial direction. We understand that the state

of stress in the plate is approximately plane stress (providing plate thickness $h \ll a$), so that $\sigma_{zz} = \sigma_{zr} = \sigma_{z\theta} = 0$. In this case the traction vector lies in the plane, with components

$$\mathbf{t} = -(\sigma_{rr}\mathbf{e}_r + \sigma_{r\theta}\mathbf{e}_\theta) = \mathbf{0}, \quad (2)$$

which is consistent with an evaluation of eq. (1) at $r = a$:

$$\sigma_{rr}(r = a, \theta) = 0 \quad (3a)$$

$$\sigma_{\theta\theta}(r = a, \theta) = \sigma (1 - 2 \cos(2\theta)) \quad (3b)$$

$$\sigma_{r\theta}(r = a, \theta) = 0 \quad (3c)$$

For $\theta = \pi/2$, the hoop stress in eq. (3b) attains its maximum value of $\sigma_{\theta\theta} = \sigma_{\max} = 3\sigma$. This corresponds to the peak of the stress distribution circumferential stress distribution shown in Figure 2a. Hence we may say that the **stress concentration factor** (the ratio of the maximum local stress [component] to the far-field stress [component]) for this geometry is equal to 3. The concept of a stress concentration factor will be further discussed in the following section. However, it is important to note that stress near the hole greatly exceeds the far-field stress. Consequently, *failure processes¹ may initiate locally at the edge of the hole under values of far-field stress which are themselves sufficiently small to preclude such failures from occurring remotely.*

Figure 2b, which shows the radial variation of $\sigma_{\theta\theta}$ along the ray $\theta = \pi/2$, emphasizes that the magnitude of the stress concentration associated with the hole decays rapidly with increasing distance from the notch. This is a clear example of **St. Venant's principle**, which states that the perturbations in a linear elastic stress field due to the presence of an isolated geometrical discontinuity of size “ d ” are localized within a region of characteristic linear dimension $\sim 3d$ from the discontinuity. The stress levels outside this region are therefore close to the nominal applied stress levels (unperturbed).

¹e.g., yielding (failure to deform only elastically), fracture (failure to remain an intact body), fatigue damage (failure to sustain load-carrying capacity over repeated load cycles) , *etc.*

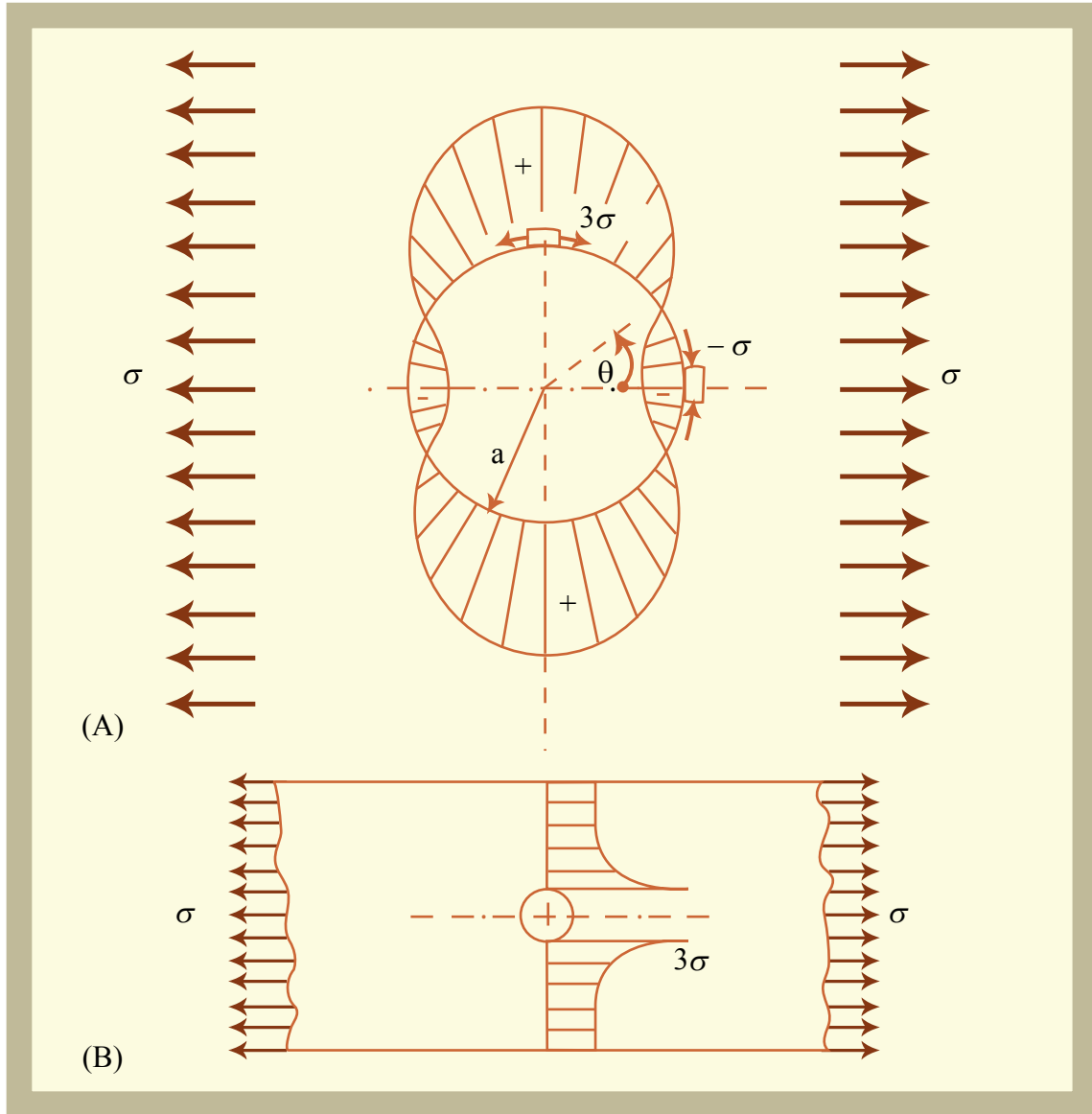


Figure 2: Distribution of hoop stress component $\sigma_{\theta\theta}$: (a) around the circumference of circular hole in a large body, and (b) radial distribution along the ligament where $\theta = \pi/2$.

5 Linear Elastic Stress Concentration Factors for Different Geometries

See also, Crandall, Dahl, & Lardner, Sections 5.9 and 5.7)

5.1 Stress concentration factors

Stress concentration factors have been obtained for several geometries of engineering significance. These are often tabulated in engineering handbooks (*e.g.*, “[R. E.] Peterson’s Stress Concentration Factors,” 2nd. Ed., John Wiley, New York, 1997, edited by W. D. Pilkey). Two types of stress concentration factor definitions are found in the literature, and it is important to apply the analysis consistent with the given definition. The first type of definition of stress concentration factor is based on the “gross” applied stress, σ_g (see equation (6) below for definition of σ_g). This stress concentration factor is given the symbol “ K_{tg} ” according to

$$K_{tg} \equiv \frac{\sigma_{\max}}{\sigma_g}, \quad (4)$$

where σ_{\max} is the maximum local stress at the edge of the hole, and σ_g is the applied far-field stress remote from the hole.

Similarly, we may also define the stress concentration factor based on the nominal (or net-section average) applied stress, σ_{nom} , according to

$$K_{tn} \equiv \frac{\sigma_{\max}}{\sigma_{\text{nom}}}. \quad (5)$$

Here σ_{nom} is the nominal, or net-section average stress acting across the minimum net area, A_{net} , of the plane containing the notch. The total tensile load, P , transmitted along a finite-sized member is finite and equal to the product of gross applied stress, σ_g , and gross area, A_{gross} ; we also require the product of nominal stress, σ_{nom} , and net-section area, A_{net} , to equal the load:

$$P = \sigma_g A_{\text{gross}} = \sigma_{\text{nom}} A_{\text{net}}, \quad (6)$$

so that

$$\sigma_{\text{nom}} = \sigma_g \frac{A_{\text{gross}}}{A_{\text{net}}}. \quad (7)$$

For example, in a uniform-thickness plate (thickness = h = constant) of width $2w$ containing a central circular hole of radius a , $A_{\text{gross}} = 2wh$ and $A_{\text{net}} = A_{\text{gross}} - 2ah$; thus $A_{\text{gross}}/A_{\text{net}} = 2wh/h(2w-2a) = 1/(1-a/w)$, so $\sigma_{\text{nom}} = \sigma_g/(1-a/w)$. Evidently, since

σ_{\max} is unique, the stress concentration factors K_{tg} and K_{tn} differ by a corresponding (but inverse!) area ratio:

$$K_{tn} = K_{tg} \left(\frac{A_{\text{net}}}{A_{\text{gross}}} \right) = K_{tg} \cdot (1 - a/w). \quad (8)$$

Values for both stress concentration measures K_{tg} and K_{tn} for centrally-located circular holes in tensile-loaded plates of finite width are given in the graph of Fig. 3; it is readily verified from the figure that eq. (8) holds. It is also clear that in the limit of a finite hole in a very large body, the distinction between “net” and “gross” stress measures and stress concentration factors vanishes.

5.2 Stress concentration for elliptical holes in ‘infinitely wide’ plates

For the case of elliptical holes in an infinitely wide plate (e.g., plate width $2w \rightarrow \infty$, $b/w \rightarrow 0$) subject to remote tensile loading, the stress concentration factor $K_{t\infty}$ can be obtained analytically, and is given by:

$$K_{t\infty} = 1 + 2 \frac{b}{a}, \quad (9)$$

where $2a$ is the length of the ellipse diameter in a direction parallel to the remote tension, and $2b$ is the length of the ellipse diameter in the direction perpendicular to the remote tension. The location of the maximum stress is at the ends of the $2b$ -axis of the ellipse. Equation (9) is plotted as a solid line in Figure 4.

Equation (9) may also be expressed as

$$K_{t\infty} = 1 + 2 \sqrt{\frac{b}{\rho}}, \quad (10)$$

where ρ is the local radius of curvature of the edge of the ellipse near the $2b$ -axis; for an ellipse, at this location, $\rho = a^2/b$.

5.3 Approximate stress concentration factors from “equivalent ellipse” models

Equation (10) may be used to estimate the stress concentration factors for other “near-ellipse” isolated hole geometries in wide plates by introducing the idea of an “equivalent” ellipse. Figure 5 illustrates the concept for three different non-elliptical notch shapes of actual tip root radius $\rho = r$ and actual length $2b$ projected perpendicular to the remote tensile axis; the “equivalent ellipse” for each notch is shown in

dotted lines, having length $2b$ and “equivalent width” in the tensile stressing direction equal to $2a_{\text{equivalent}} = 2\sqrt{br}$.

Use of the equivalent ellipse concept then allows an estimation of the maximum stress at the root of the isolated near-elliptical notch, for remote applied stress “ σ^∞ ,” as

$$\sigma_{\text{max}} \doteq \sigma^\infty \times K_{t\infty}(b, a_{\text{equivalent}}) = \sigma^\infty \times \left(1 + 2 \frac{b}{a_{\text{equivalent}}}\right). \quad (11)$$

Image removed due to copyright considerations. See Chart 4.50 in Pilkey, Walter. Peterson's Stress Concentrations, 2nd ed. New York: Wiley, 1992.

Image removed due to copyright considerations. See Chart 4.1 in Pilkey, Walter. Peterson's Stress Concentrations, 2nd ed. New York: Wiley, 1992.

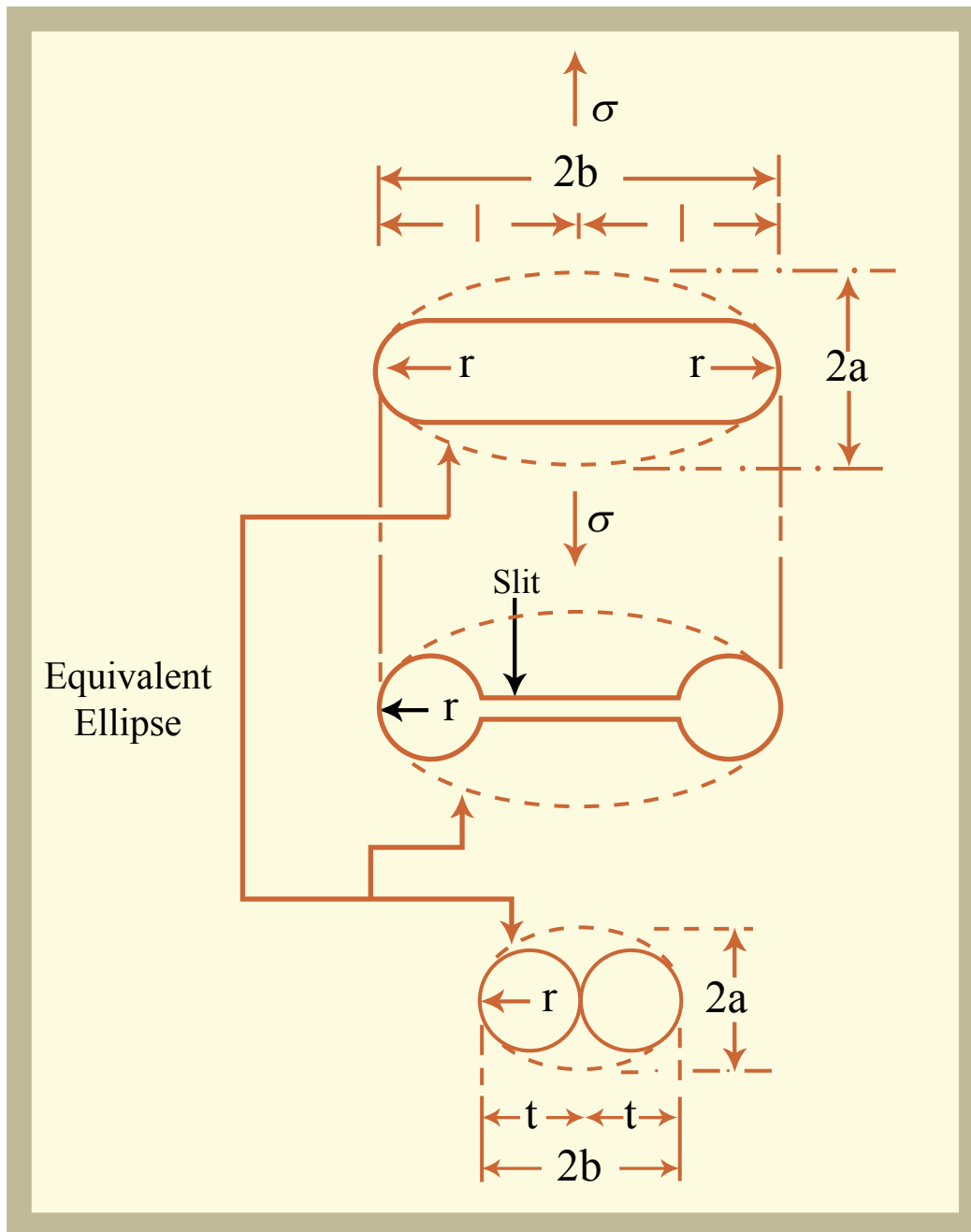


Figure 5: Schematic illustration of “equivalent ellipse” concept for various isolated notch geometries under remote tension. The notch root radius is denoted “ r ” in the figure, while it is termed “ ρ ” in eq. (10). Note that the top geometry of the slot is one of those tested in the polycarbonate plate in this lab (see Figure 8b).

6 Introduction to Photoelasticity

NOTE: this section provides qualitative description [only!] of photoelastic stress analysis procedures.

Stress distributions in some transparent materials may also be measured using photoelastic techniques. These rely on illumination with plane polarized light obtained by passing light rays through vertical slots that produce polarized light beams having waves that oscillate only along one plane perpendicular to the travel of the light ray. When the polarized light passes through a material which is being stressed in a direction parallel to the polarizing axis, then a fringe pattern is formed against a light (bright field) background. Conversely, when the stress axis is perpendicular to the polarizing axis, a “dark field”, or black image is formed.

In some materials, the application of stress may cause an incident plane-polarized ray to split into two coincident rays with directions that coincide with the directions of the in-plane principal stress directions. Since this phenomenon is only observed during the temporary application of stress, it is known as “temporary birefringence”. Furthermore, the speeds of the rays are proportional to the magnitudes of the respective principal stresses. Hence, the emerging rays are out of phase. They therefore produce interference fringe patterns when they are recombined. If they are recombined at an analyzer (shown in Fig. 6), then the amount of interference in the emerging rays is directly proportional to the difference between the local in-plane principal stress levels, σ_p and σ_q . therefore, the amount of interference is related to the maximum in-plane shear stress, which is given by

$$\tau_{\max} = \frac{1}{2} (\sigma_p - \sigma_q). \quad (12)$$

The fringe patterns therefore provide a visual indication of the spatial variations in the maximum in-plane shear stress.

Quantitative information on local principal/maximum shear stress levels may also be obtained from the fringe patterns. The difference in the levels of maximum shear stress at any two points, $\Delta\tau_{\max}$, is proportional to the number of fringes, n , between the two points. The proportionality constant depends on the thickness of the planar body, h , and a fringe coefficient, f , characteristic of the birefringent material:

$$\Delta\tau_{\max} = \frac{nf}{h}. \quad (13)$$

The value of f for a given material may be determined from a stress calibration experiment on a geometry for which the stress distribution is known *a priori*.

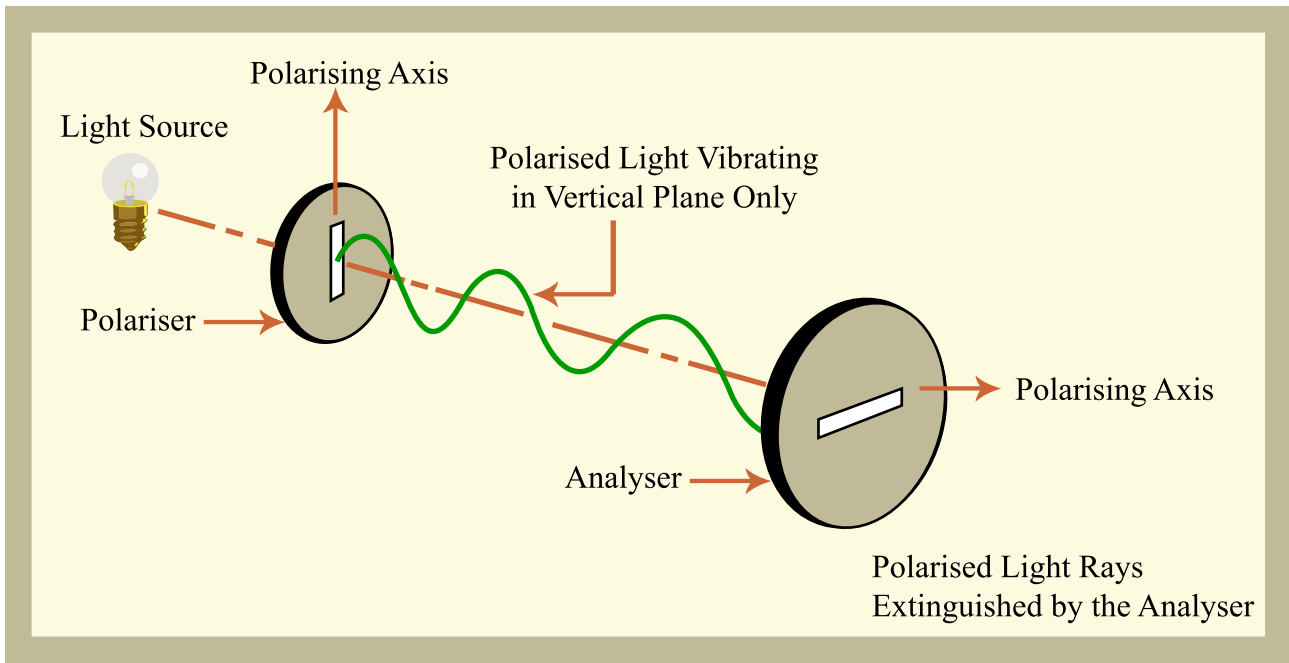


Figure 6: Schematic of polarizer and analyzer set-up.

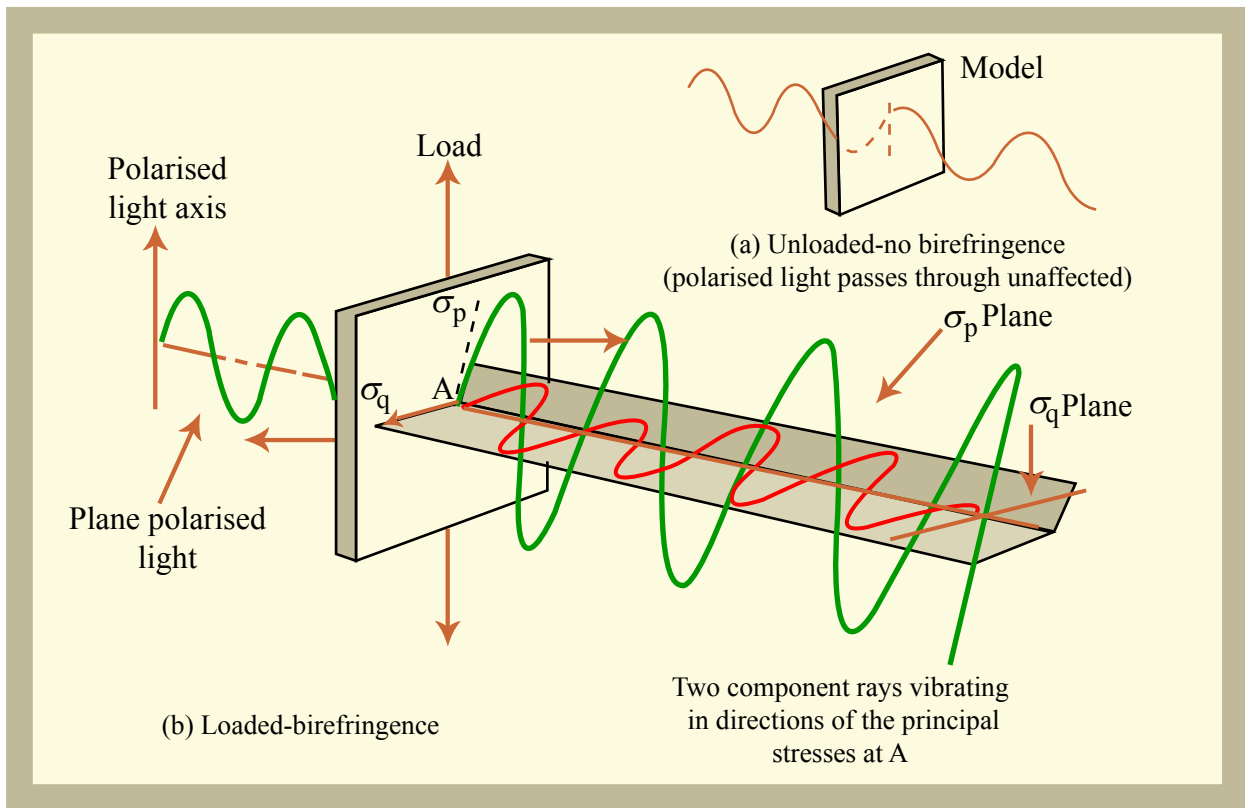


Figure e: Temporary birefringence. (a) Plane-polarised light directed onto an unstressed model passes through unaltered. (b) When the model is stressed the incident plane-polarised light is split into two component rays. The directions of the rays coincide with the directions of the principal stresses, and the speeds of the rays are proportional to the magnitudes of the respective stresses in their directions. The emerging rays are out of phase, and produce an interference pattern of fringes.

Figure 7: Interaction of polarized light with loaded specimen prior to recombination after passing through analyzer .

7 Experimental Procedure

Two experiments will be performed in this lab. In the first experiment, an aluminum plate of thickness h and width $2b$, with a central circular hole of diameter $2a$ (see Figure 8a), will be subjected to elastic-level tensile load of magnitude P . Strain distributions will be measured using strain gauges attached to different positions on the plate. Local tangent strains, $\epsilon_{\theta\theta}$, will be measured at five positions (gauges #1, 2, 3, 5, and 8, as detailed in Figure 9) along the ligament. An additional, remotely-located strain gauge (#10 in Fig. 9), oriented parallel to the loading direction, will be used to obtain measurements of axial far-field strain. Exact positions of the gauges with respect to the hole are given in Fig. 9.

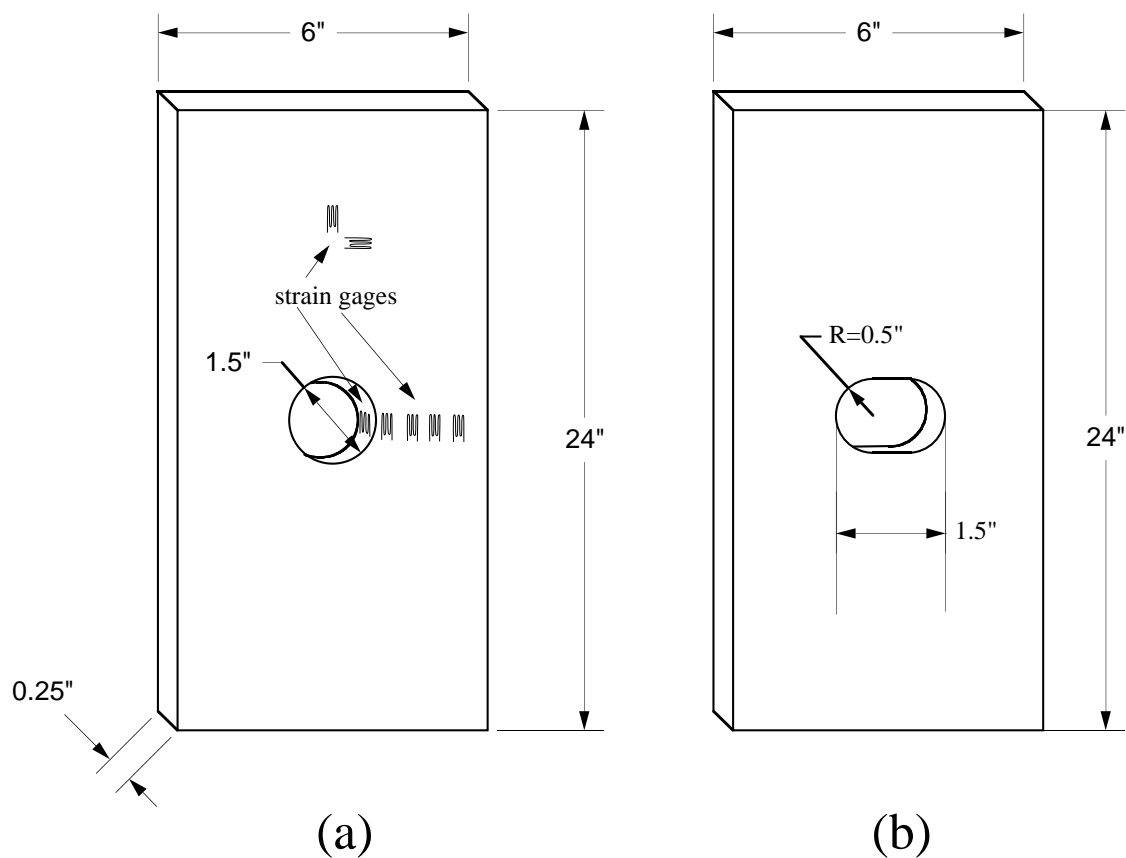


Figure 8: Geometry of the plates tested in this module. (a) Plate with a circular hole: both an aluminum and a polycarbonate plate of this geometry will be tested. In the figure, the positions of strain gauges applied to the aluminum specimen are schematically indicated. Precise gauge locations are shown in Fig. 9. (b) Polycarbonated plate with a slot.

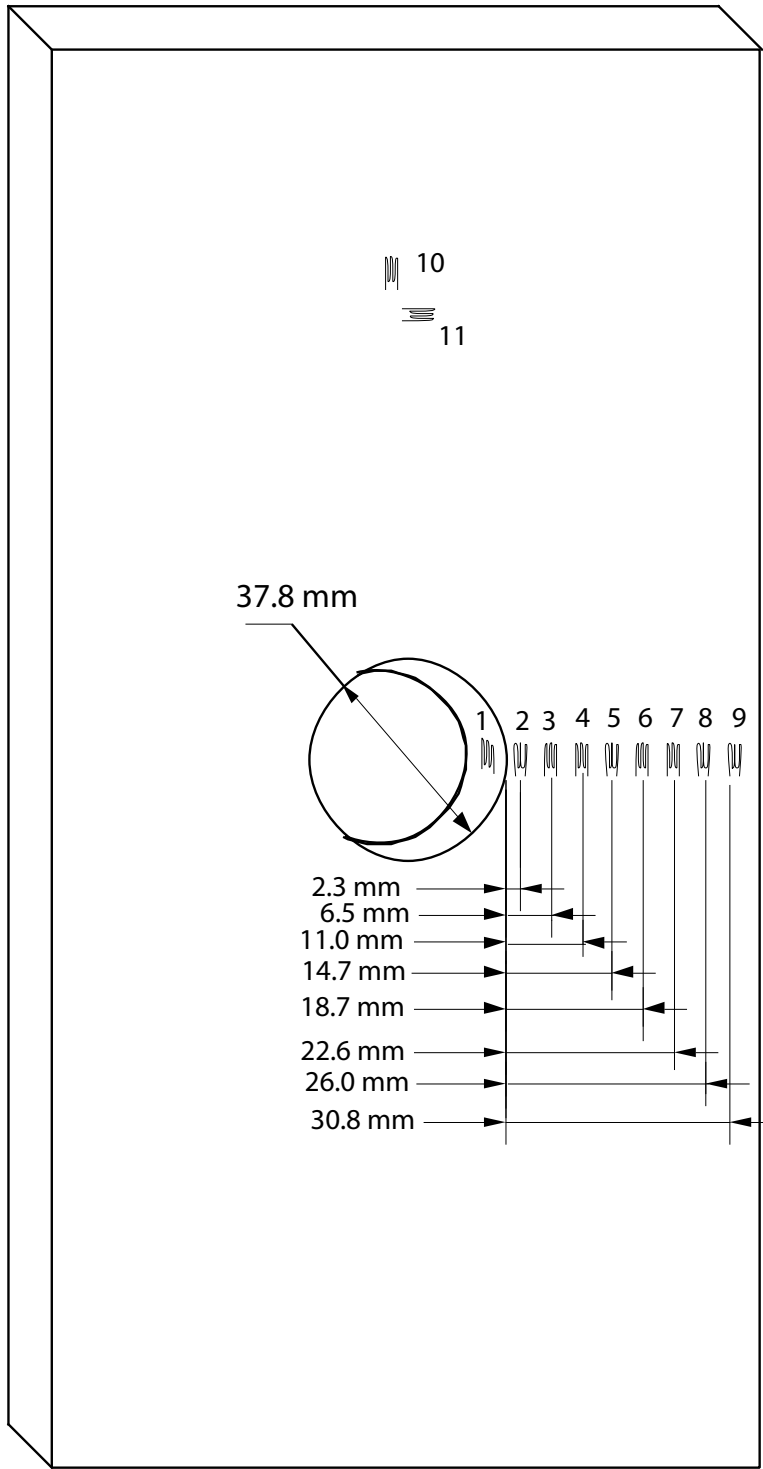


Figure 9: Positions of the strain gauges on the aluminum plate.

An experimental measure of the strain concentration factor, K_ϵ , can then be computed from the ratio of the maximum local strain at the notch root, ϵ_{\max} , to the remote axial strain, ϵ_{axial} :

$$K_\epsilon = \frac{\epsilon_{\max}}{\epsilon_{\text{axial}}}. \quad (13)$$

Note that for this geometry, with purely elastic behavior and uniaxial tensile stress states, both locally on the notch surface and remotely, $K_\epsilon = K_{tg}$.

In the second experiment, a plate made of a transparent polymer, polycarbonate (PC), will be subjected to tensile loading. The geometry of the plate is identical to that of the aluminum specimen, except that it also contains a wide and narrow slot located above the circular hole. Birefringence patterns will be observed on the loaded plate using the set-up shown in Fig. 7. However, no attempt will be made to quantify the stress distributions associated with the fringe patterns. Instead, the fringes will be examined qualitatively to determine the approximate sizes of regions of stress concentration in the vicinity of the notch. The fringe patterns will also be examined to verify the applicability of the St. Venant principle.

8 Numerical Stress Analysis: Finite Element Solutions

Today, most quantitative stress analysis is conducted using powerful computer techniques; the most widely-used of these is the **finite element method**. In applications to isotropic linear elasticity, the method constructs an approximate (but [with sufficient care!] numerically accurate) solution to the equations governing elastic boundary value problems. In practice, the approximate displacement field is constructed as a piecewise-continuous, low-order polynomial within small (but finite) “elements;” in two-dimensional models (e.g., plane stress), the elements are typically triangular or quadrilateral-shaped. Figure 10 shows a mesh of quadrilateral elements used here to model the hole-in-plate tension specimen.

As part of the output of the approximate solution, we can obtain color contour plots of the spatial variation of particular stress components. Figure 11 shows a detail of the variation of stress component σ_{22} when the far-field load is $P = 10 \text{ kN}$, leading to a [remote] gross stress of $\sigma_{\text{gross}} = P/2bh = 10.33 \text{ MPa}$ (plate thickness is $h = 6.35 \text{ mm}$; total plate width is $2b = 152.4 \text{ mm}$; hole diameter is $2a = 38.1 \text{ mm}$); Figure 12 shows a similar variation of shear stress component σ_{12} .

The contour plots can also be “sectioned” along a given path within the material, to plot the variation of a particular variable along that path. Figure 13 plots the “radial” variation (variation in direction x_1) of normalized stress component σ_{22} across the minimum ligament at the horizontal center-plane of the specimen. The local stress

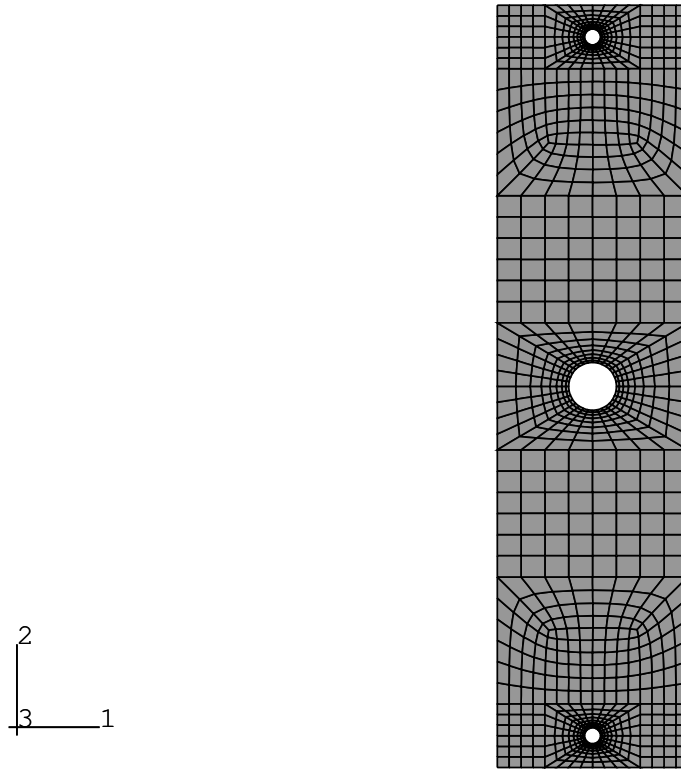


Figure 10: Finite element mesh used to generate approximate stress analysis solution.

is normalized by the remote gross stress, $\sigma_g = P/2bh$. The peak value at the root of the hole is 3.26, dropping to 0.904 at the edge of the specimen. Figure 14 plots the normalized strain component ϵ_{22} over the same region; here strain is normalized with remote gross strain, $\epsilon_g = \sigma_g/E$.

Commercial finite element packages typically have a large number of capabilities to enable experienced users to perform precise mechanical and thermal analysis in problems of great complexity; accordingly, the user-interfaces to these powerful packages often have substantially steep “learning curves.” We will be exploring use of the finite element method with “pdetool”, a MATLAB-based finite element package of limited capability, but with a simple and intuitive user interface. The software can be accessed within the MATLAB command window by issuing the command ‘pdetool’. More information on pdetool will be provided in lecture.

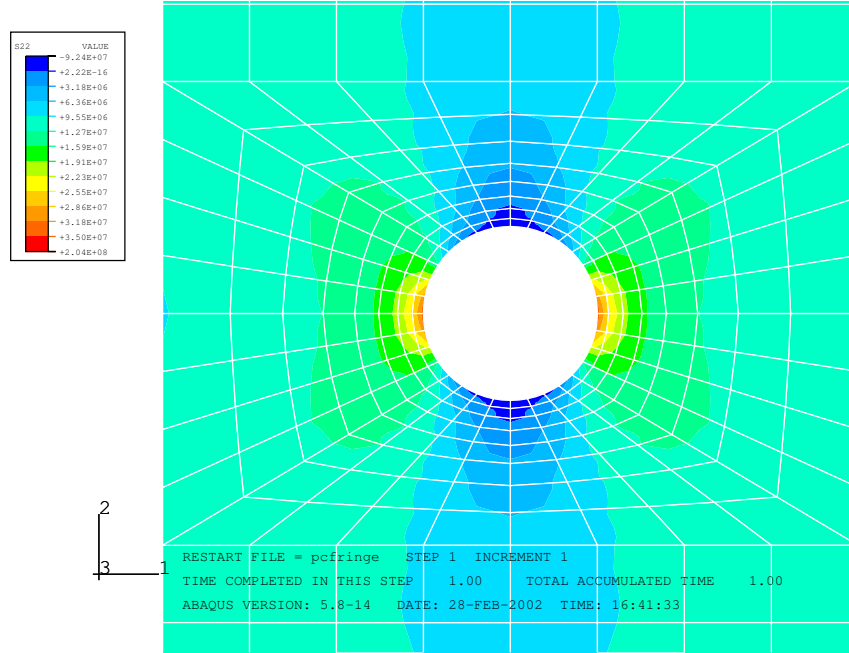


Figure 11: Contour plots of axial stress component σ_{22} . Remote (gross) stress level is $\sigma_{22}^{\infty} = P/(2bh) = 10.33 \text{ MPa}$.

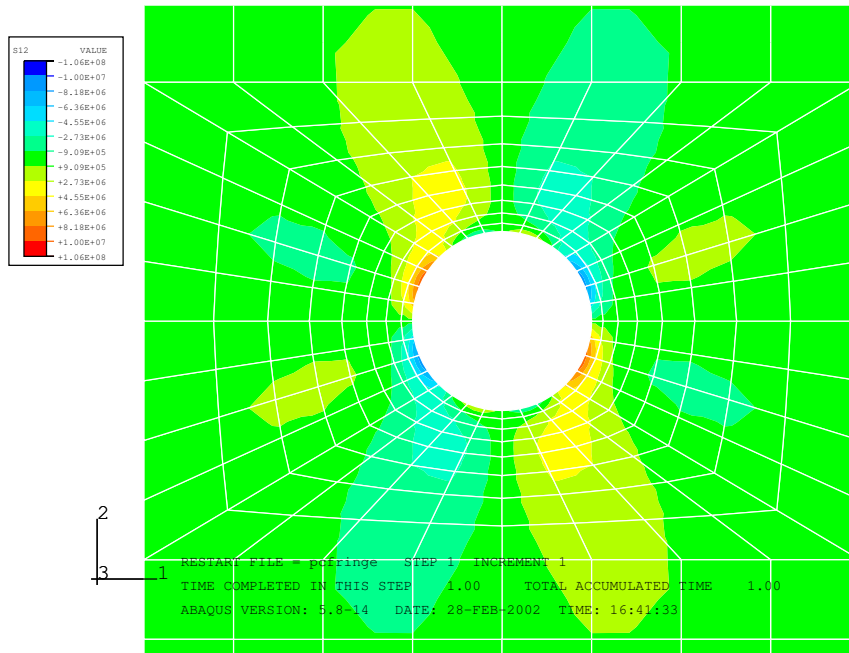


Figure 12: Contour plots of shear stress component σ_{12} . Remote (gross) stress level is $\sigma_{22}^{\infty} = P/(2bh) \equiv \sigma_g = 10.33 \text{ MPa}$.

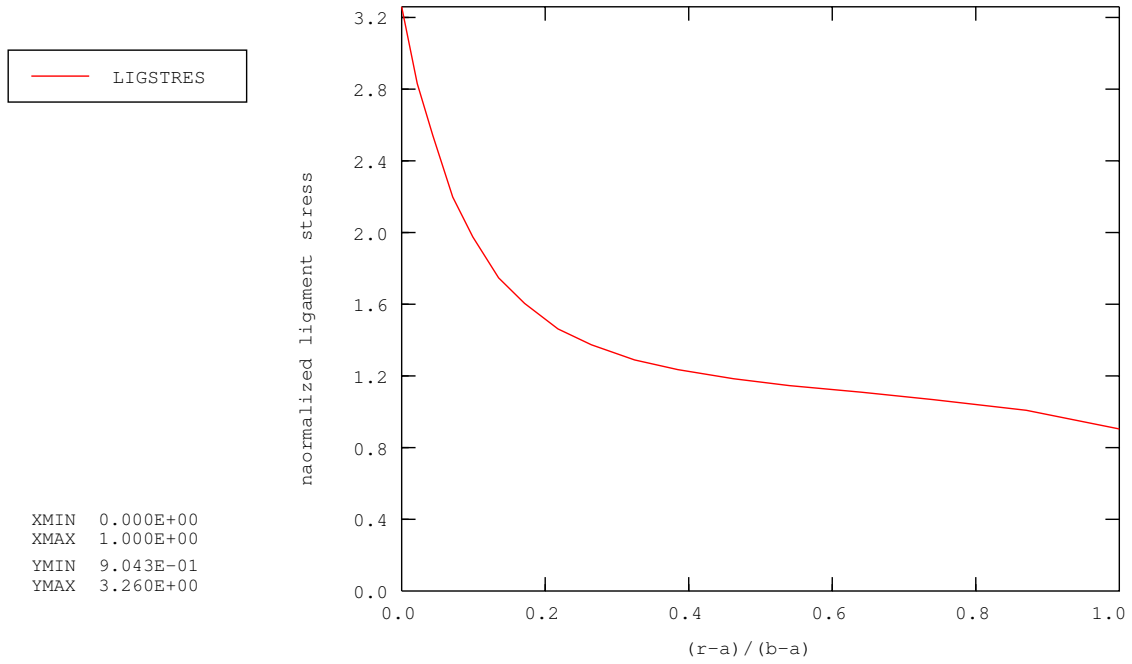


Figure 13: Normalized stress distribution along minimum ligament. Normalization is $\sigma_{22}/(P/2bh)$ vs. normalized ligament coordinate $(r - a)/(b - a)$.

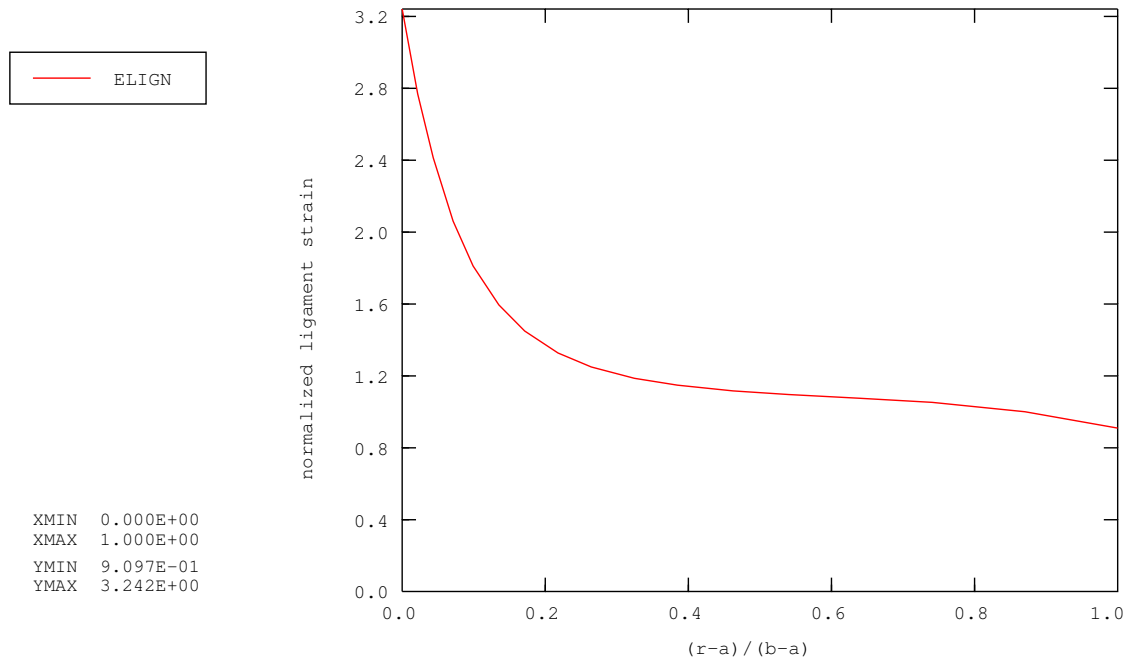


Figure 14: Normalized strain distribution along minimum ligament. Normalization is $\epsilon_{22}/(P/2Ebh)$ vs. normalized ligament coordinate $(r - a)/(b - a)$.